Journal of Crystal Growth 575 (2021) 126353

Contents lists available at ScienceDirect

Journal of Crystal Growth

journal homepage: www.elsevier.com/locate/jcrysgro

Theoretical and experimental study of $(Ga_{1-x}Fe_x)_2O_3$ ternary alloys

Md Dalim Mia [a,*], Brian C Samuels [a], Md Abdul Ahad Talukder [a], Pablo D. Borges [c], Luisa Scolfaro [a], Wilhelmus J. Geerts [a], Ravi Droopad [a,b]

[a] Materials Science, Engineering & Commercialization (MSEC) Program, Department Physics, Texas State University, San Marcos, TX 78666, USA
[b] Ingram School of Engineering, Texas State University, San Marcos, TX 78666, USA
[c] Universidade Federal de Vicosa, Rio Paranaiba, MG, Brazil

ARTICLE INFO

Communicated by T. Paskova

Keywords:
A1. Alloys of iron gallium oxide
A2. $(Ga_{1-x}Fe_x)_2O_3$
A3. Ultrawide bandgap
A4. X-Ray diffraction
B1. DFT calculations
B2. Ferromagnetism
B3. Optical Properties
B4. Pulsed laser deposition

ABSTRACT

Thin films of Ga_2O_3 and its alloys open the possibility of ultrawide bandgap heterostructure device designs that includes HEMT, quantum well UV optoelectronics, wide bandgap spintronics, high resistive buffer layers for FET and electrocatalytic applications. In this paper, $(Ga_{1-x}Fe_x)_2O_3$ (for x = 0.0–0.50) thin film alloys as a function of growth temperatures (450–750 °C) and partial oxygen pressures (10^{-1} – 10^{-6} torr) grown using pulsed laser deposition are reported. The results suggest that, with the increase of Fe content at a fixed growth temperature and pressure, the bandgap decreases (4.93 to 3.43 eV and 4.39 to 2.25 eV for direct and indirect, respectively) due to a change in the Fe oxidation states as the Fe composition is increased from 0 to 50%. Density functional theory calculations also show a reduction in the bandgap of the alloy as the Fe content increases with the formation of a localized band of states close to the conduction band. Fe content, ≥ 40% in the alloy leads a phase change in the crystal structure with the formation of a gamma phase, also corroborated by theoretical calculations. Finally, room temperature ferromagnetic property was observed in thin films with the introduction of Fe into the Ga_2O_3 lattice.

1. Introduction

Ultrawide bandgap Ga_2O_3 and its alloys having bandgaps > 4.6 eV, a predicted high breakdown field (6-8MVcm ^{1}), and a high electron saturation velocity (2×10^{7} cm/s), have been propelling investigations into versatile applications such as gas sensors, transparent conductive oxides for solar cells, UV detectors, magnetic sensors and devices, high-power electronic devices (including MOSFETs) and electrocatalytic energy production [1–4] It's proven capability of growing high-quality single crystals from melt offer huge potential for cost effective large scale device manufacturing [5–7]. However intrinsic β-Ga_2O_3 often suffers from n-type conductivity due to the unintentionally incorporated defects in the crystal [8]. Consequently a high off-state drain leakage current and the absence of a sharp pinch-off [9] in electronic devices during operation is problematic. In lateral field effect transistor (FET) applications, a key building block is the formation of a high resistivity buffer layer. Therefore, for power application, a highly insulating β-Ga_2O_3 layer achieved either by doping or alloying is needed. The most common way to achieve highly resistive Ga_2O_3 material is through doping by divalent atoms (Mg^{2+}, Be^{2+}, Zn^{2+} and Fe^{2+}) into the lattice in which the atoms substitute into the trivalent Ga sites [10–13]. There have been relatively few studies of the effect of Fe in β-Ga_2O_3. Fe is believed to form deep state acceptor levels which increase the resistivity of the material [14–17]. Hence, Fe doping of Ga_2O_3 can potentially be a good candidate for the formation of a highly insulating homoepitaxial crystalline buffer layers or as a suitable gate dielectric in MOSFET applications.

In addition to highly insulating layers that can result from Fe doping of Ga_2O_3, there has also been growing interest in Fe doped Ga_2O_3 to achieve wide bandgap diluted magnetic semiconductor oxides for spintronic applications [18–22]. Fe can be incorporated into Ga_2O_3 by replacing the Ga atoms and it is expected to have similar oxidation state. However, Fe can readily exist in a 3+ and 2+ oxidation states and in the ternary alloy there is a possibility that the growth conditions will determine which oxidation state will be dominant and its effect on the properties of the alloy. The properties of bulk $(Ga_{(1-x)}Fe_x)_2O_3$ prepared by various techniques such as float zone, sol gel, ball milling, and solid state reaction method have been reported [21–27] showing the presence of magnetic properties. In contrast, very few reports of thin films of $(Ga_{(1-x)}Fe_x)_2O_3$ ternary alloys are seen in the literature dealing with

* Corresponding author.
E-mail address: m_m880@txstate.edu (M.D. Mia).

https://doi.org/10.1016/j.jcrysgro.2021.126353
Received 27 March 2021; Received in revised form 14 August 2021; Accepted 13 September 2021
Available online 21 September 2021
0022-0248/

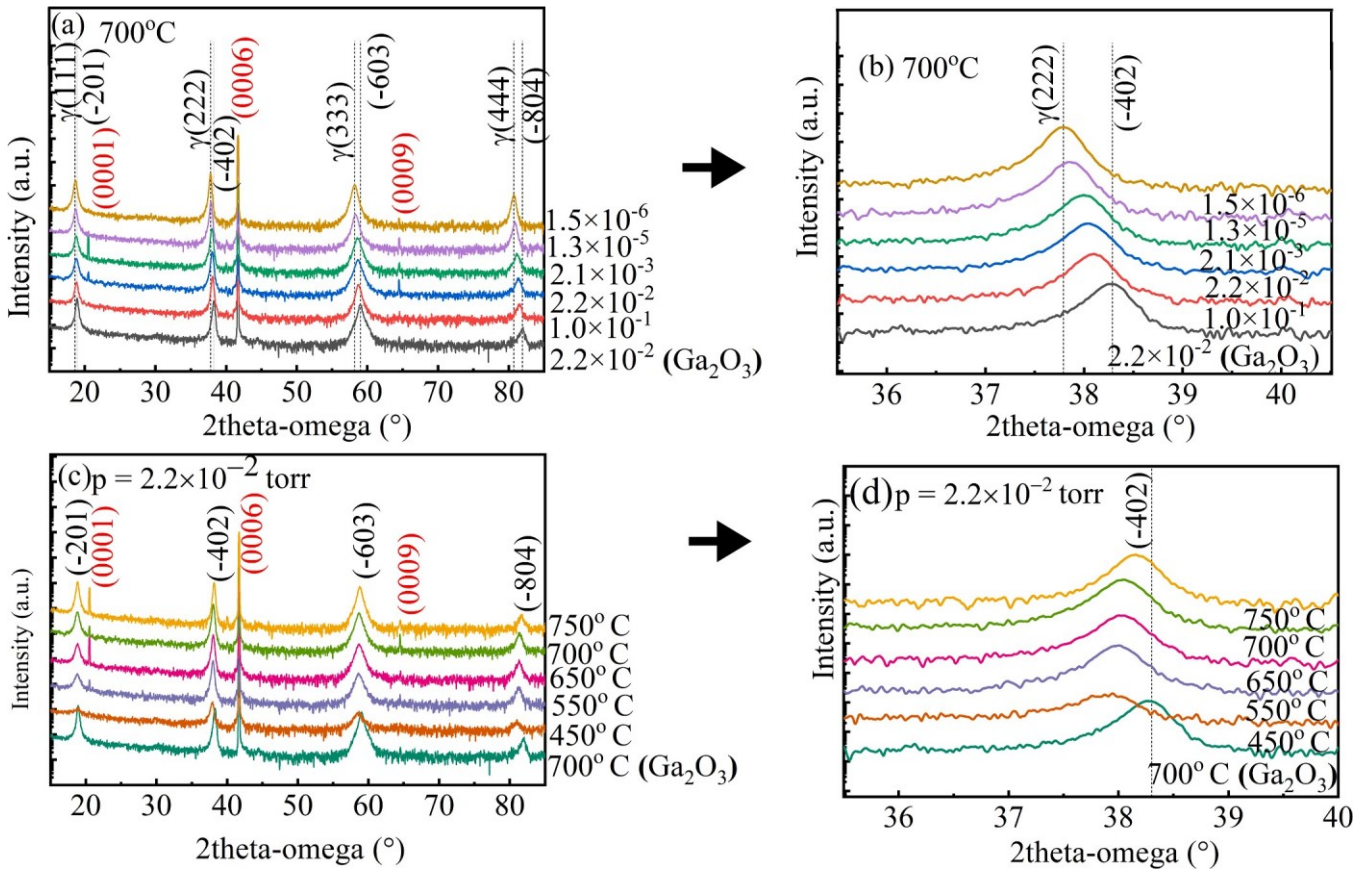

Fig. 1. 2-theta-omega scan of $(Ga_{(1-x)}Fe_x)_2O_3$ thin films for x ~ 0.15 (a) as a function oxygen partial pressure during deposition pressure at 700 °C, (b) corresponding extended region around angle 38°, (c) as a function of deposition temperature with a fixed oxygen partial pressure of $2.2x10^{-2}$ torr, (d) corresponding extended region around angle 38°.

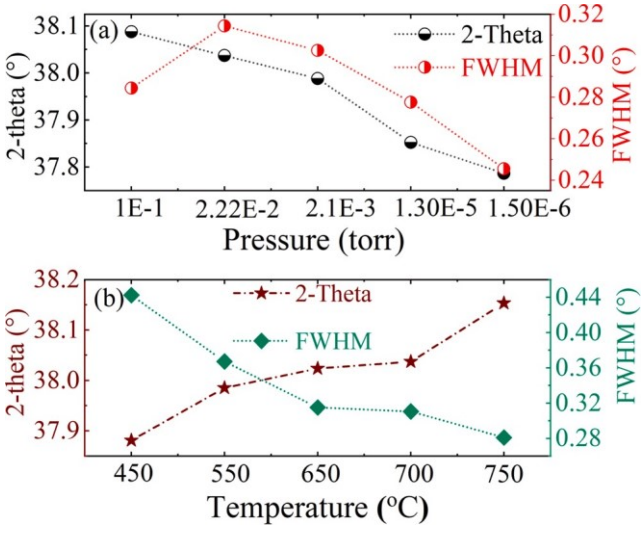

Fig. 2. (a) FWHM and 2-theta versus partial oxygen pressure, (b) FWHM and 2-theta versus deposition temperature of $(Ga_{0.85}Fe_{0.15})_2O_3$ thin films.

magnetic properties [20,28–34]. Most of the prior studies of $(Ga_{1-x}Fe_x)_2O_3$ thin films were focused on high Fe concentration materials (typically × > 0.5) with limited studies on low Fe content. Daoyou Guo et al. [33] demonstrated ferromagnetic properties of monoclinic $Ga_2O_3/(Ga_{1-x}Fe_x)_2O_3$ (x = 2.44%) thin film on sapphire substrates deposited using laser molecular beam epitaxy (LMBE). However, instead of a deposition of a uniform alloy, the alloy was achieved by the alternating deposition of Ga_2O_3 and Fe layers and using high temperatures to allow for the interdiffusion of the layers. In this study thin films with an Fe content from 0 to ~ 50 % were studied and it was reported that the Fe in these films exhibit mixed valence states of Fe^{2+} and Fe^{3+}. Yuanqi Huang et al. [35] demonstrated ferromagnetism in the cubic structure of Fe stabilized γ-Ga_2O_3 thin films grown on c-plane sapphire substrates and suggested possible application in nonvolatile magnetic storage devices. These Fe doped γ-Ga_2O_3 films were deposited using LMBE at low oxygen pressure (chamber pressure ~ 10^{-7} torr) and Fe content < 10%. Ferromagnetism in orthorhombic GaFeO thin films were also studied on ITO buffered YSZ(001) [30], $SrTiO_3$(111)[19], and $SrRuO_3$(111) [20]. Ferromagnetism in combination with a transparent semiconductor oxide is promising since the ferromagnetic properties can be tuned by light [36–38] making this material interesting for optoelectronics applications with novel magneto-optical devices properties [39,40].

Extensive studies of $(Ga_{1-x}Fe_x)_2O_3$ thin film alloys as a function of growth conditions and Fe concentration have not been explored in the literature. In this work, a systematic investigation of $(Ga_{1-x}Fe_x)_2O_3$ thin films as a function of growth parameters will be presented including structural, electronic, optical, and magnetic properties. These results will be compared with density functional theory (DFT) studies.

2. Experimental and computational details

2.1. Experimental process details

$(Ga_{1-x}Fe_x)_2O_3$ thin films for x ~ 0.15 were first grown at various temperatures (400–750 °C) and oxygen pressures (1.5×10^{-6} torr ~ 2.2×10^{-2} torr) to study the effect of temperature and pressure on the crystallinity and the structure of the films. Following this study, a fixed

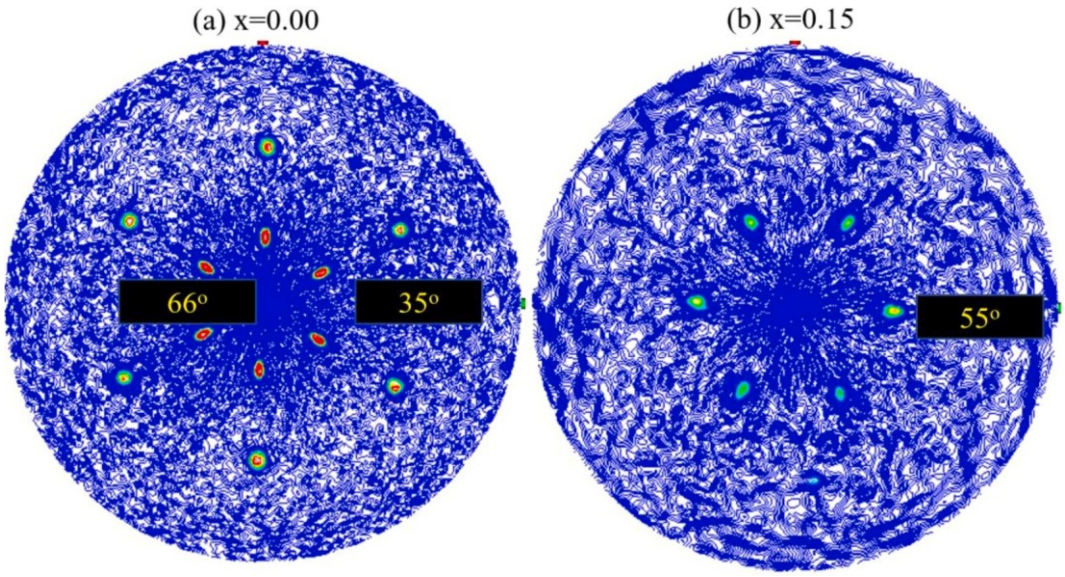

Fig. 3. X-ray PF measurement of $(Ga_{(1-x)}Fe_x)_2O_3$ thin films for (a) x = 0.00 and (b) x = 0.15 were grown at partial oxygen pressures 2.2×10^{-2} and 1.5×10^{-6} torr, respectively, at fixed temperature 700 °C.

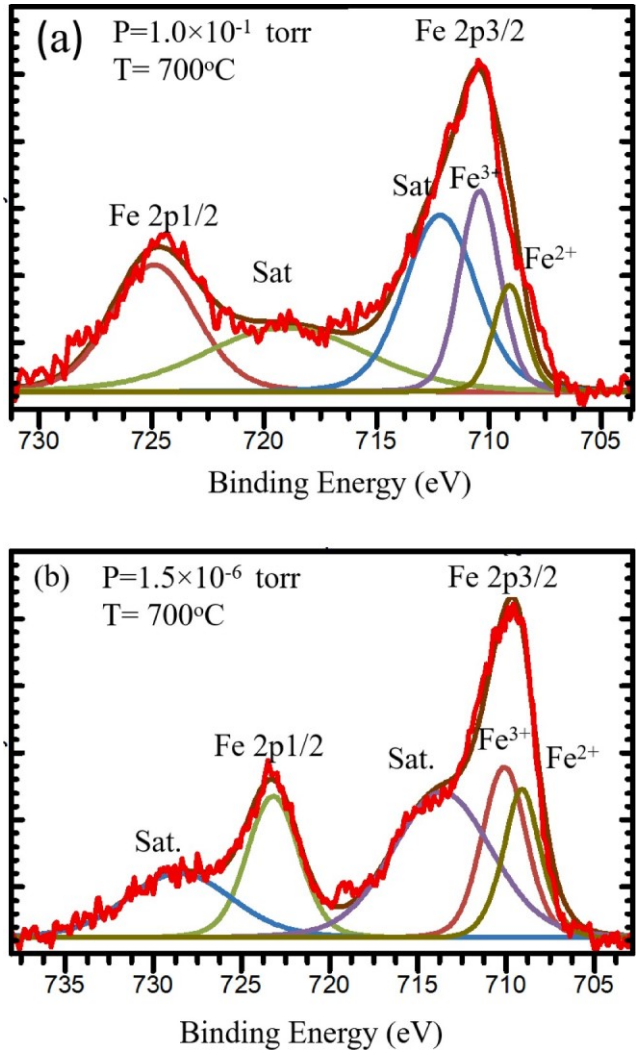

Fig. 4. Core level Fe 2p XPS spectrum of $(Ga_{(1-x)}Fe_x)_2O_3$ thin films for x = 0.15 at a pressure of (a) pressure 1.0×10^{-1} torr (b) 1.50×10^{-6} torr.

growth temperature of 700 °C and oxygen partial pressure of 2.2×10^{-2} torr were used to grow a series of $(Ga_{1-x}Fe_x)_2O_3$ films having different Fe content (x). All films were grown using pulsed laser deposition (PLD) on single sided polished c-plane sapphire substrates. The substrates were cleaned ultrasonically using acetone, isopropanol, deionized water and finally dried with nitrogen gas prior to loading into the load lock. After growth, each film was annealed for 15 min at a temperature of 50 °C above the growth temperature in the absence of oxygen. The targets used for deposition were fabricated from 5 N Ga_2O_3 and 5 N Fe_2O_3 powders with varied Fe (mole ratio of Fe/(Ga:Fe)) concentration. A krypton fluoride (KrF) excimer laser source having a wavelength of 248 nm was used to ablate the target onto the substrate. During deposition, the laser pulse frequency was set at 5 Hz and the beam was set to an energy density of 2 J/cm^2. The rotation of the substrate, target, and the distance between them were carefully controlled to maintain film uniformity and to prevent crater formation on the target.

2.2. Theoretical computational modelling

The calculations performed during this study were based on first-principles spin-dependent density functional theory (DFT) [41,42]. The projector augmented-wave basis as implemented in the Vienna ab-initio Simulation Package (VASP) [43], and the generalized gradient approximation (GGA) in conjunction with the Perdue-Burke-Ernzerhof (PBE) exchange-correlation functional [44] was used. To account for the electron-electron and exchange coupling interactions of the valence Fe *d*-states, the effective Hubbard potential approach (GGA + U) with the U value 3.84 eV was used. This value of U was determined in accordance with Ref. [45] by dividing the calculated atomic Hubbard potential by the Ga_2O_3 dielectric constant. For undoped β-Ga_2O_3, calculations were carried out using a modified Becke-Johnson *meta*-GGA potential (GGA + mBJ) [46]. The β-Ga_2O_3 has a monoclinic crystal structure with space group C2/m. The calculated lattice constants for β-Ga_2O_3 were a = 12.474 Å, b = 3.088 Å, c = 5.886 Å, and the calculated angle β = 103.684°, obtained by minimizing the total energy of the unit cell using GGA, are in good agreement with the experimental values reported in the literature [47]. The lattice constants are kept fixed in the optimized GGA values, shown above, when performing calculations using other functionals (GGA + mBJ, GGA + mBJ + U).

The $(Ga_{1-x}Fe_x)_2O_3$ alloys were simulated using a 20-atom supercell, in which Ga atoms were replaced by Fe atoms simulating the different ×

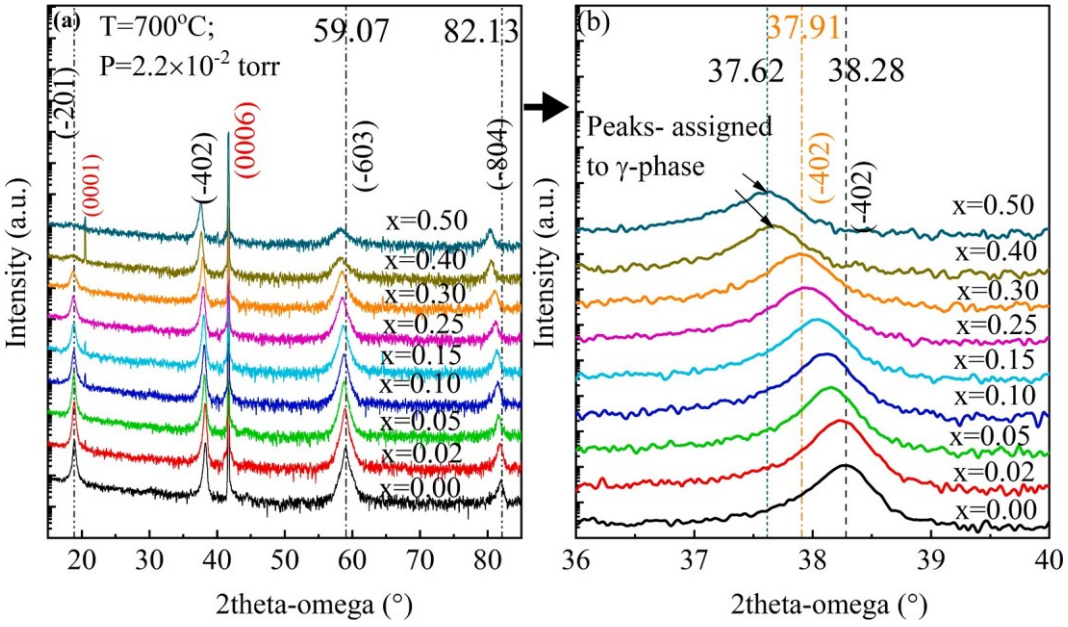

Fig. 5. (a) X-ray diffraction patterns of films $(Ga_{(1-x)}Fe_x)_2O_3$ grown at 700 °C and 2.2 × 10^{-2} torr oxygen as a function of Fe content. (b) expanded view of the spectra around angle 38°.

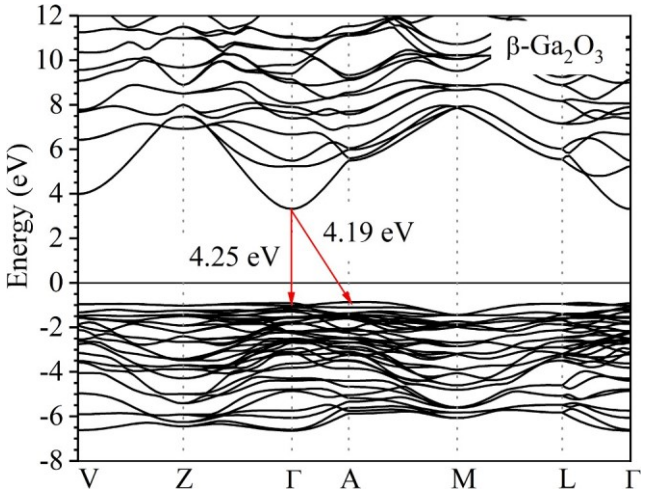

Fig. 6. Band structure calculated for β-Ga_2O_3, using the GGA + mBJ functional, along high-symmetry lines in the Brillouin zone. The indirect and direct band gaps are indicated by arrows. The Fermi level is placed at the zero energy.

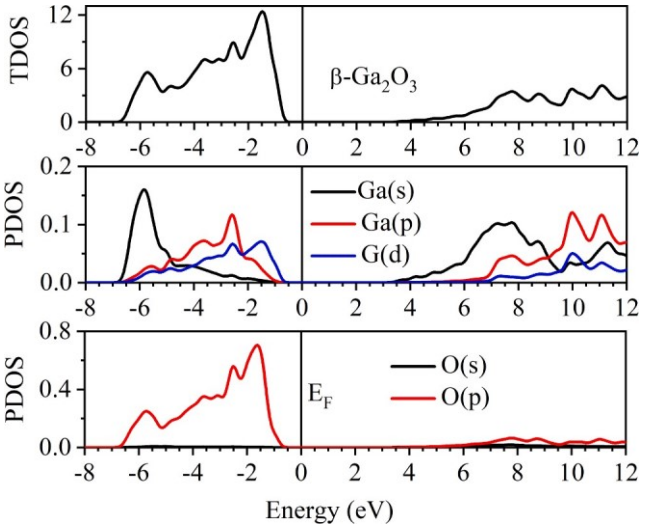

Fig. 7. Total density of states (TDOS) and projected density of states (PDOS), per atomic orbital, calculated for β-Ga_2O_3, using the GGA + mBJ functional. The Fermi level is placed at the zero energy.

values studied, x = 0, 0.125, 0.25, and 0.50. The β-Ga_2O_3 comprises two types of Ga atoms, Ga^1 corresponding to octahedral (OCT) sites, and Ga^2, which correspond to the tetrahedral (TET) sites. Ferromagnetic (FM) and anti-ferromagnetic (AFM) configurations for Fe were also investigated. The AFM configuration is found to be the most stable, independent of Fe either replacing Ga on the OCT site or the TET site. All structures were relaxed, allowing for the stabilization of the atomic positions until the forces on the atoms were dropped to 10^{-5} eV/ Å. The self-consistent calculations used a (2× 8 ×4) k-points mesh to represent the reciprocal space. Calculations were performed using a collinear spin-polarized approach with a kinetic energy cutoff of 450 eV for the plane-waves basis set. For the density of states calculations, a (✱ 16 × 8) k-points mesh was used.

For the cubic spinel phase of the 50% Fe concentration, the simulation was carried out using the Fd-3 m (#227) structure model representing $Fe_{1.25}Ga_{1.75}O_4$ to investigate the stability of the systems under compressive and tensile strain. A supercell was built, containing 56 atoms, with 8 Fe atoms in tetrahedral sites, 16 Ga atoms in octahedral sites, and 320 atoms. The pristine crystal structure can be represented as $Fe_8Ga_{16}O_{32}$originated from the γ-phase $Ga_{24}O_{32}$ spinel structure with eight Ga_3O_4 unit cells [33]. In terms of the total number of cations the structure consists of 50% Fe and 50 % Ga in the supercell, that is, $Fe_{12}Ga_{12}O_{32}$, where 4 gallium atoms were replaced by 4 iron atoms. Thus, in this simulation, 8 Fe atoms continue to occupy octahedral sites with the additional 4 Fe atoms occupying the tetrahedral sites. The lattice parameter was optimized to be 8.363 Å, as shown in Fig. 10. This result is comparable with the experimental value reported for spinel $FeGa_2O_4$, 8.363 Å. [48]

3. Results and discussion

Fig. 1 shows the XRD 2θ/ω spectra of $(Ga_{(1-x)}Fe_x)_2O_3$ thin films for x

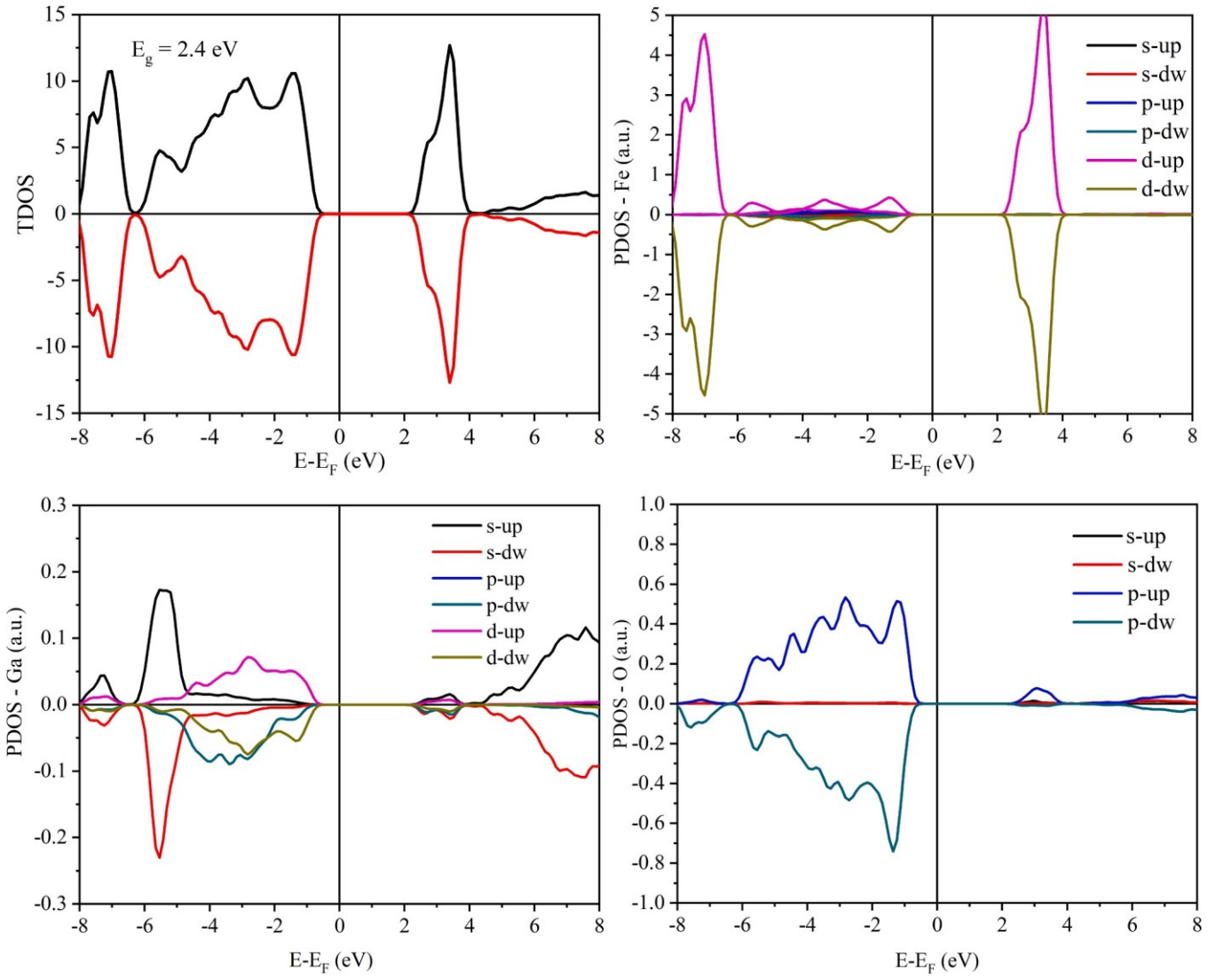

Fig. 8. Total (T) and Partial Density of States (PDOS) per atom for ß-$(Ga_{(1-x)}Fe_x)_2O_3$, with Fe concentration of 50 %, calculated using GGA + mBJ + U. Fermi energy is placed at the zero energy. Arbitrary units for density of states and energies are in eV.

= 0.15 as a function of deposition temperature and oxygen partial pressure. Fig. 1(a) represents oxygen partial oxygen pressure dependency, and 1(b) is the enlarged regions around the diffraction angle of 38°. All sample peak positions were compared with the baseline undoped ß-Ga_2O_3 grown at T = 700 °C and P_{O2} = 2.2 × 10^{-2} torr. The sharp peaks at 20.5°, 41.7° and 64.5° correspond to the diffraction peaks of the (0003), (0006) and (0009) planes of the sapphire substrate. It is clearly observed that with the decrease of oxygen pressure, the peaks related to the thin film shift towards lower 2theta angle, without any degradation of the crystal quality (Fig. 1a, b). The lowest full width half maxima (FWHM) was observed for an O_2 pressure of 1.5 × 10^{-6} torr shown in Fig. 2(a). The shift in the peak around 38° to lower 2theta is not due to a change in the film composition but would suggest a change in the crystal phase as a result of a change in the oxidation states of the cations. To fully investigate this phenomenon, pole figure (PF) and XPS measurements were carried out. Analysis of the PF data suggests that for $(Ga_{0.85}Fe_{0.15})_2O_3$ a phase transformation to a cubic (gamma) ɣ-phase occurs with lower oxygen partial pressure as shown in Fig. 3. Before taking PF measurement, the diffraction angle was set at 2□=29.5°. It is seen that there is a six-fold symmetry for x = 0.0 for tilt angles around 35° and 66° that can be attributed to the (−400) and (401) Bragg's planes of the monoclinic phase. The six-fold symmetry is maintained for the x = 0.15 sample but diffraction peaks only appear at a tilt angle around 55°. These peaks can be assigned to the (220) plane of the cubic or ɣ-$(Ga_{(1-x)}Fe_x)_2O_3$ crystal structure. The monotonic shift in the lattice constant with decreasing oxygen content used during growth can be explained by an increase in the amount Fe^{2+} ions in the film (as discussed below). The peaks at 18.59°, 37.81°, 58.18° and 80.70° displayed in the 2θ/ω spectrum of the x= 0.15 deposited at low oxygen partial pressure are due to diffraction of the (111), (222), (333) & (444) planes of ɣ-$(Ga_{(1-x)}Fe_x)_2O_3$, respectively. The data in Fig. 1b would therefore suggest that as the oxygen partial pressure is decreased during deposition there is a higher fraction of the gamma phase over the beta phases present in the film with the lowest oxygen partial pressure producing a complete gamma phase. This change in the crystal phase is due to the change in oxidation states of the Fe as will be discussed later. Similar observations were made by Y. Huang *et al.* [35] who deposited $(Ga_{(1-x)}Fe_x)_2O_3$ thin films for × = 0, 5.38, and 9.62 at% on (0001) sapphire substrates at an O_2 partial pressure of ~ 7.5 × 10^{-8} torr and temperature of 750 °C using PLD. Their films were annealed postgrowth at 750 °C for 1 h in vacuum. Fig. 1 (c) and (d) show the 2θ/ω XRD spectra of $(Ga_{(1-x)}Fe_x)_2O_3$ thin films for x =0.15 grown at a O_2 pressure of 2.2 × 10^{-2} torr as a function of growth temperature. It is seen that for higher growth temperatures there is an improvement in the crystallinity which is confirmed by a smaller FWHM of (402) plane shown in Fig. 2b. Interestingly, a low deposition temperature causes the peak to

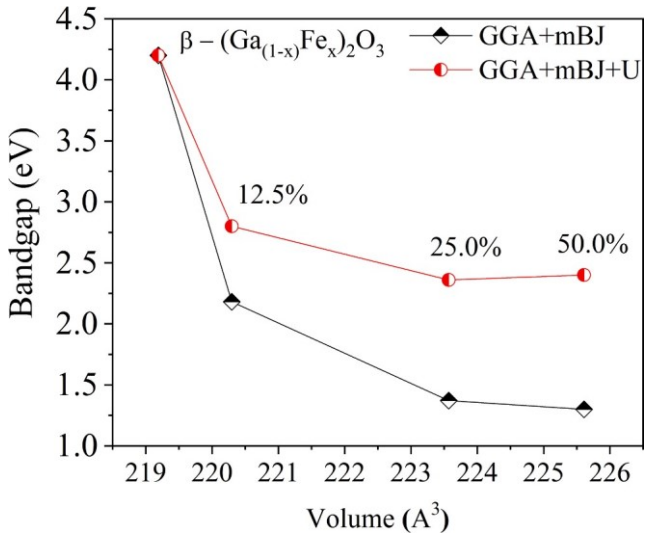

Fig. 9. Band gap energy variation as a function supercell volume, for β-$(Ga_{(1-x)}Fe_x)_2O_3$ for x = 0, 0.125, 0.25, 0.50. Calculations performed with the GGA + mBJ functional and with the GGA + mBJ + U functional are indicated by the symbols "squares" and "circles" respectively. Volumes correspond to fully relaxed calculations for each Fe composition. Solid lines connecting the symbols are to guide the eyes.

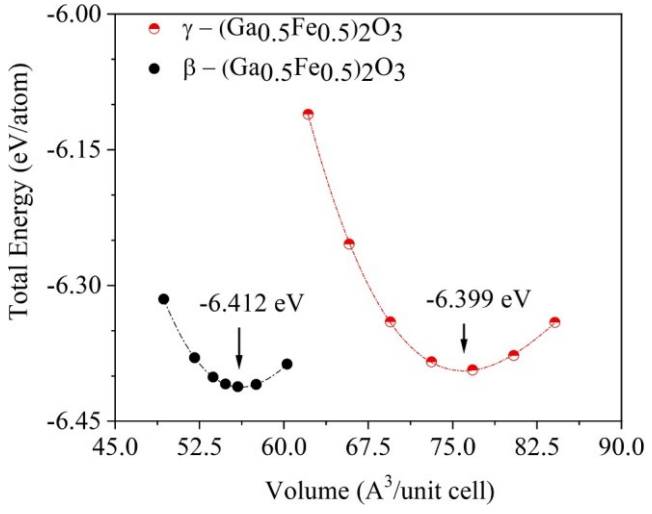

Fig. 10. Total energy versus volume, as obtained for $(Ga_{0.5}Fe_{0.5})_2O_3$ in the β (circles) and for $Fe_{1.25}Ga_{1.75}O_4$ in the γ (triangles) structural phases, using the GGA + U functional. The total energy values at the minimum volume of each structure are indicated by vertical arrows.

shift to smaller angles representing an increase of lattice constant but with degraded crystallinity. This can be explained by an increase in the Fe^{2+}/ Fe^{3+} ratio for films deposited at lower temperatures. Note that Fe^{2+} (0.74 Å) has larger ionic radius than Fe^{3+} (0.64 Å) and Ga^{2+} (0.62 Å) [49–33]. To confirm whether this is true, XPS measurements were performed to estimate the Fe^{3+}/Fe^{2+} ratio in the $(Ga_{0.85}Fe_{0.15})_2O_3$ grown at two different partial oxygen pressures. The Fe 2p core level XPS spectra are shown in Fig. 4a and 4b for growths under oxygen partial pressures of 1.0×10^{-1} torr and 1.5×10^{-6} torr, respectively. The XPS peak positions were calibrated using the C 1 s peak at the binding energy of 284.8 eV and the Fe $2p_{3/2}$ main peaks was deconvoluted into Fe^{3+} and Fe^{2+} peaks [51], corresponding to the binding energy around 710.42 eV and 709.06 eV, respectively. The ratio of Fe^{3+}/Fe^{2+} is about 2.37 and 1.95 for partial oxygen pressure 1.0×10^{-1} and 1.5×10^{-6} torr, respectively, confirming that increasing the oxygen pressure during growth result in a higher concentration of Fe^{3+}. In addition to core the level peaks Fe $2p_{1/2}$ and Fe $2p_{3/2}$, satellite peaks are observed due to the spin orbit coupling indicated by Sat. in Fig. 4 which are due to a sudden change in the Coulombic potential as the emitted electron passes through the valence band. The differences in satellites peaks in Fig. 4 appears to be due to the presence of varying amounts of Fe^{3+} [52,53,54]. These XRD and XPS result are in agreement with the results of Y. Huang et al. [17], who studied the temperature and oxygen pressure dependence of a much lower Fe content (equivalent to x = 2.5%) $Ga_{1.95}Fe_{0.05}O_3$ thin films. In conclusion, the change in crystal phase from beta to gamma observed in Fig. 1 is due to change in the Fe oxidation from Fe^{3+} to Fe^{2+} as the oxygen partial pressure during deposition is reduced. This change of phase is also confirmed from the pole figure measurements.

From an analysis of the above data, a growth temperature of 700 °C and oxygen partial pressure of 2.2×10^{-2} torr was chosen to investigate the effect of the Fe concentration on the growth of $(Ga_{1-x}Fe_x)_2O_3$ thin films. Samples were grown for x = 0.0–0.50 and were subjected to a post deposition anneal at 750 °C for 15 min in the PLD growth chamber after having stopped the flow of oxygen. The 2θ/ω XRD spectra for these samples are shown in Fig. 5. For x=0, in addition to the substrate peaks prominent sharp peaks representing the Bragg reflections of the (−201), (402), (603) and (804) planes for a monoclinic β-Ga_2O_3 thin film that is grown on the c-plane sapphire substrates are present. Fig. 5 (b) shows an enlarged view of the spectra around the diffraction angle of 38° for the various samples. This figure shows that with increasing Fe concentration, the (402) diffraction peak gradually shifts to smaller angles, suggesting an expansion of the lattice constants due to an increasing amount of Fe inclusion into Ga_2O_3 lattice sites [55,56]. However, as clearly seen, increasing Fe content also degrades the structural quality of the thin films at these deposition conditions. While there is a monotonically increase in the lattice constant with increasing Fe content up to x=0.30, the peak positions for the alloys with x = 0.40 and 0.50 suggest the existence of the spinel phase that is reported elsewhere [35,57,58]. The peaks at approximately 38°, 58° and 80° can be indexed as the (222), (333) and (444) diffractions plane of γ phase thin films, representing the spinel phase of the $(Ga_{(1-x)}Fe_x)_2O_3$ alloy. The missing (111) peak may be due to the degraded crystal structure, i.e., the temperature and oxygen partial pressure used may not be ideal for growing high quality spinel phase for these high Fe content films.

Fig. 6 shows the calculated band structure along high symmetry lines of the Brillouin zone (BZ) for undoped β-Ga_2O_3, obtained using the GGA + mBJ functional. Fig. 7 depicts the corresponding total density of states (TDOS) and projected density of states (PDOS), per atomic orbital. The bandgap obtained from this calculation is approximately 4.25 eV (direct) and 4.19 eV (indirect). These values show good accordance with those obtained using the computationally most expensive PBE0 approach (not shown) [59] and other previous theoretical calculations [8,60]. The band structure of β-Ga_2O_3 consists of a flat valence band, indicating a large hole effective mass, which implies a low hole mobility and poses a challenge to fabricating p-type β-Ga_2O_3. From the density of states results, the bandgap consists of contributions from Ga(s), Ga(p), Ga(d) and O(s) orbitals. To check the electronic properties of the β-$(Ga_{(1-x)}Fe_x)_2O_3$ alloy, Fe atoms were added to the β-Ga_2O_3 structure replacing Ga atoms for varying x from 0.0 to 50%. The calculated results suggest that the incorporation of Fe into the lattice causes the volume of the unit cell to increase while at the same time the bandgap shrinks. The presence of Fe is responsible for introducing a rather localized band in the upper part of the band gap close to or at the CB bottom, consistent with previous DFT studies for 12.5 % Fe content in Ga_2O_3 using the local density approximation (LDA) [61]. Here we found the Fe *d*-derived states located at ~ 2.4 eV above the VB top, and about 1.5–2 eV wide, for the Fe concentration x = 0.5 as shown in Fig. 8. For all x values studied, we found Fe in the AFM configuration to be the most favorable compared with the FM configuration, and for several different

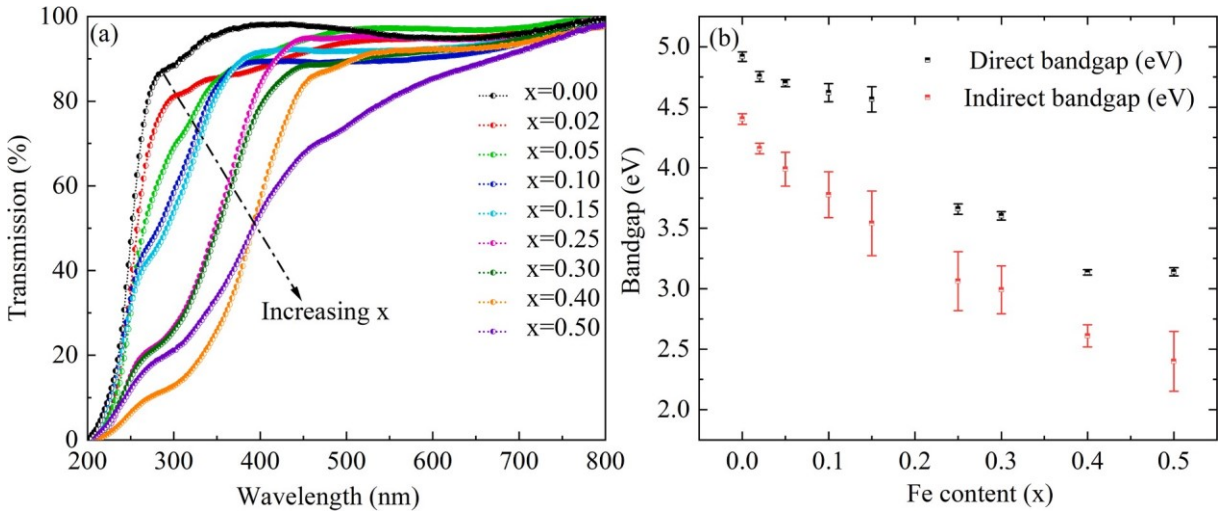

Fig. 11. (a) Optical transmission spectroscopy of the various as-grown alloys and (b) direct and indirect transition for $(Ga_{(1-x)}Fe_x)_2O_3$ thin films extracted from the Tauc plot.

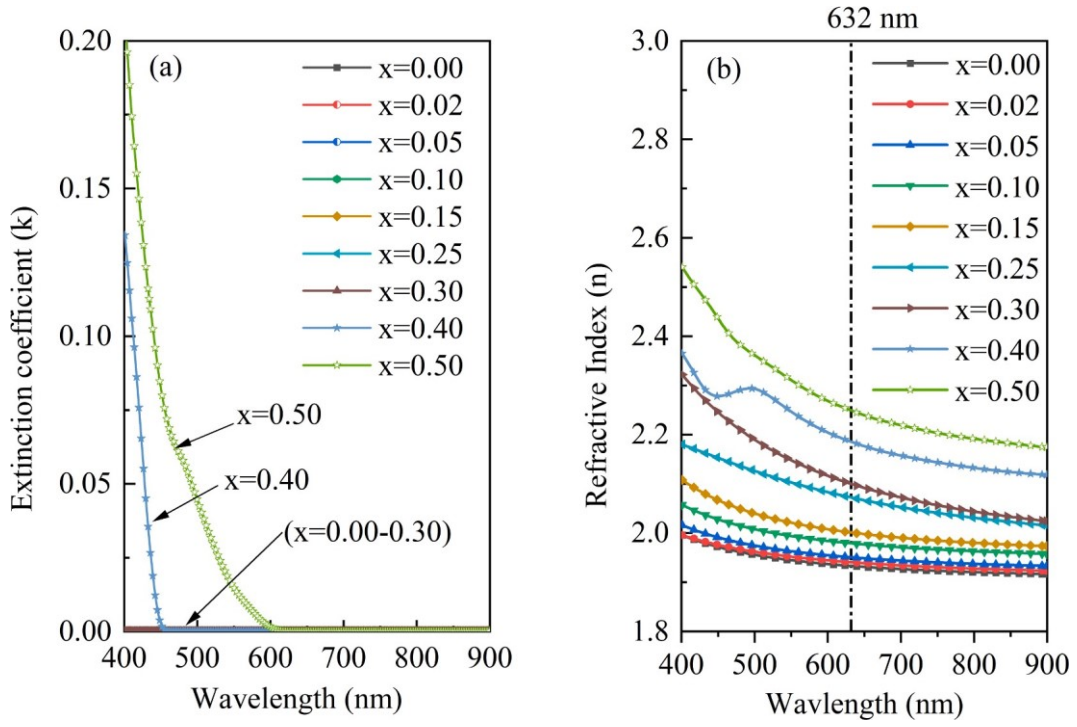

Fig. 12. (a) Extinction coefficient and (b) refractive index as function of wavelength for $(Ga_{(1-x)}Fe_x)_2O_3$ thin films for various Fe content.

arrangements of the Fe atoms in the Ga_2O_3 supercell. We point out, however, that in few cases where the Fe atoms are more than two atomic layers apart from each other the total energy difference between the AFM and FM configuration is smaller than 5 meV. This finding may lead the FM configuration to be competitive with the AFM one, especially for diluted alloys.

In Fig. 9 we show the band gap energy variation as the supercell volume increases, for films β-$(Ga_{(1-x)}Fe_x)_2O_3$ for x = 0, 0.125, 0.25, 0.50, comparing results obtained from calculations performed with the GGA + mBJ functional and those with the GGA + mBJ + U functional. The reduction of the bandgap is consistent with the experimental optical transmission data shown in Fig. 11 below.

Moreover, we observe that the inclusion of the mBJ potential, added to the + U Hubbard potential for iron is fundamental to correctly describe not only the trend in the band gap energy as × increases, but also its magnitude. To better understand the stability of the alloys under the effect of strain, we varied the lattice constants around the minimum equilibrium volume of the $(Ga_{(1-x}Fe_x)_2O_3$ alloy for x= 0.50. Fig. 10 presents the total energy as function of the unit cell volume for β-$(Ga_{0.5}Fe_{0.5})_2O_3$ and γ-$(Ga_{0.5})Fe_{0.5})_2O_3$. These results show that the monoclinic phase is the most stable by only 13 meV, at least for 50% Fe content in the alloy. However, the experimental observation of cubic phase in the high Fe content $(Ga_{1-x}$ $Fe_x)_2$ O_3 samples is not unexpected considering the small energy difference between the two structures and the calculation does not consider the oxidation states of the Fe atoms. We add that although the absolute value of the undoped Ga_2O_3 bang gap (4.25 eV, direct band gap) is found about 13% smaller than the experimental values range (4.7–4.9 eV) [7,9], the overall trend observed for

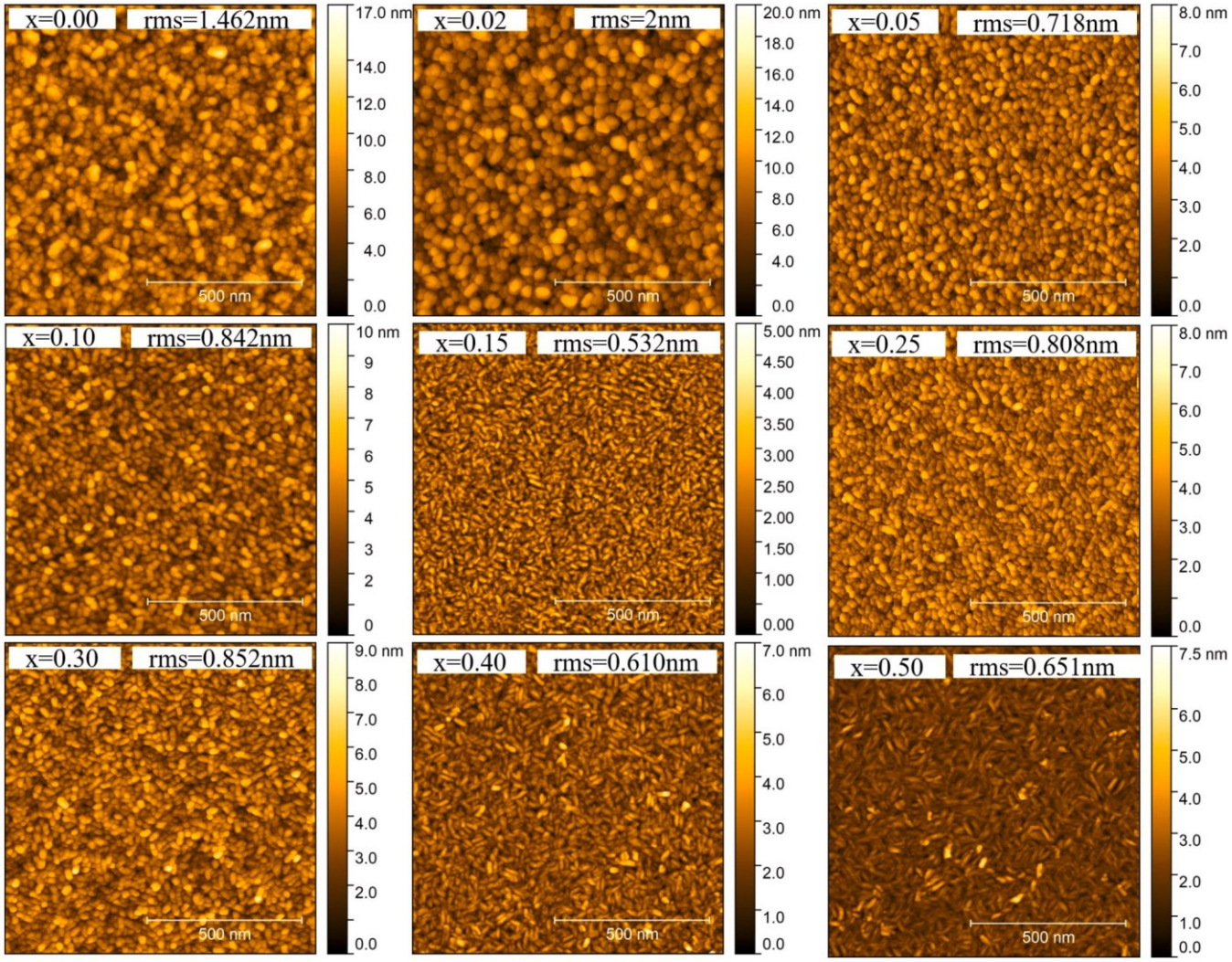

Fig. 13. AFM (1um × 1um) surface images for different Fe content in the $(Ga_{(1-x)}Fe_x)_2O_3$ alloy grown at 700 °C and 2.2 × 10^{-2} torr.

Table 1
Materials properties of $(Ga_{1-x}Fe_x)_2O_3$ at pressure 2.2 × 10^{-2} torr and temperature 700° C.

Fe content (x)	Thickness (nm)	Bandgap (eV) fm UV-vis		Refractive index at 632 nm	Roughness from Ellipsometer (nm)	RMS Roughness using sAFM (nm)
		Direct	Indirect			
0.00	106.48	4.93	4.39	1.9330	3.070	1.462
0.02	131.22	4.71	4.14	1.9406	3.400	2.000
0.05	143.19	4.67	3.96	1.9508	1.800	0.718
0.10	96.930	4.58	3.62	1.9790	1.350	0.842
0.15	82.920	4.56	3.54	2.0012	1.000	0.532
0.25	94.640	3.68	2.78	2.0724	1.200	0.808
0.30	80.540	3.60	2.75	2.1001	1.190	0.852
0.40	95.070	3.40	2.50	2.1857	0.800	0.610
0.50	52.770	3.43	2.25	2.2494	0.300	0.651

doped $(Ga_{(1-x}Fe_x)_2O_3$ systems prevails, independent of the exchan- ge- correlation functional used, explaining consistently the experimental data.

Fig. 11a shows the optical transmission spectroscopy spectrum of the $(Ga_{(1-x)}\ Fe_x)_2\ O_3$ thin films for x = 0.0 ~ 0.50, deposited at 700 °C and 2.2 × 10^{-2} torr oxygen partial pressure. β-Ga_2O_3 exhibits a high transparency over 90% with no intermediate absorption and the transmission rapidly decreases around 250 nm. To estimate the direct and indirect bandgap from the measured transmission spectra the Tauc equation $(\alpha hv)^{1/n} = B\ hv\ E_g)$ was used, where n = 1/2 and 2 for determining the direct and indirect energy band transition, hυ is the photon energy, α is the absorption coefficient and B is a constant. Fig. 11b shows the calculated direct and indirect bandgap as a function of the Fe content. The bandgap appears to decrease with Fe content which is consistent with the calculations shown in Fig. 9 suggesting that indeed the volume of the unit cell increases with Fe content. Films for x = 0.40 and x = 0.50 showed the lowest optical transparency and unlike β-Ga_2O_3, intermediate absorption appears in the alloys of $(Ga_{(1-x)}Fe_x)_2O_3$, which implies indirect transition at this thermodynamic condition, consistent with the theoretical calculations discussed below. The presence of intermediate

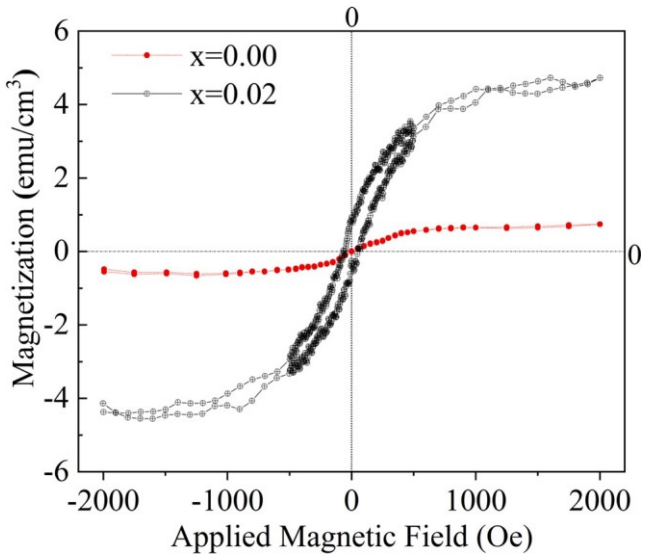

Fig. 14. M H Curve of $(Ga_{(1-x)}Fe_x)_2O_3$ thin films for Fe content x = 0.00, 0.02 taken at room temperature.

bands has potential applications in designing solar cell capable of absorbing photons with lower energy than the bandgap of the original host semiconductor utilizing electron transition from valence band or deep level defect to intermediate band, as well as the conventional process of transition from valence to conduction band. Such systems can be beneficial over the single gap solar cells, as well in applications of multi-wavelength photodetectors [62–65].

To determine the thickness and roughness and investigate further the optical properties of the thin films, spectroscopic ellipsometry measurements was carried out on the as-grown samples. The extracted parameters are shown in table I and Fig. 12. In general, the thin films have some region of optical transparency, i.e., vanishing imaginary part where the extinction coefficient approaches k = 0. This transparent region can be analyzed to extract the index of refraction and the thickness of the film by the Cauchy Sellmeier equation [66].

$$n(\lambda) = a + \frac{b}{\lambda^2} + \frac{c}{\lambda^4} \quad (1)$$

where n is the refraction index, λ is wavelength, and a, b, c are optical constants. Therefore, to determine the thickness and refraction index (at 632 nm), data sets were evaluated using the Cauchy function in the transparent spectral region. This was followed a B-spline analysis was used to obtain the optical parameters of the absorbing film. For x = 0.40 and x = 0.50, (as the absorption edges shifted above 400 nm) where Kramers-Kronig relationship was maintained by evaluating values of extinction coefficient k and the refractive index, n. From Fig. 12, it is seen that the extinction coefficient is almost zero for all sample up to 400 nm. However, for x=0.40 and 0.50 strong absorption appears at shorter wavelength, indicating bandgap shrinkage. The appearance of a dip in the spectrum around 450 nm can be attributed to absorption due to defects or intermediate band. It is also evident that the refraction index increases with Fe content. For x=0.4 and 0.5 the estimated refractive index at 632 nm are 2.1857 and 2.2494 respectively These values are greater than the refractive index (1.89 ~ 1.95) of β-Ga_2O_3 [67–70]. However, the refractive index of gamma gallium oxide in the visible region which is reported to be 2.0 ~ 2.1[71], closely matches the value obtained from the ellipsometry data, confirming the alloy structure could be the gamma phase.

The influence of Fe content on the surface morphologies (Fig. 13) and roughness (Table 1) of the films was examined using scanning atomic force microscopy (sAFM). The film surfaces are granular in nature and uniform in appearance. The surface topologies or grains size are likely related to Fe content and changes from circular to elongated rice like granules as the Fe content increases suggesting a directional dependence ad-atom migration on the surface. Increasing the growth temperatures will most likely increase the migration of the species and will probably decrease the surface roughness. The decrease in the rms values and the grain size with increasing Fe content is probably due to a decrease in the surface adatom migration in the presence of Fe and/or lack of oxygen with the increasing Fe content which pins the grain boundaries and limits the adatom mobility.

All the films presented in this study were insulating and electrical properties could not be determined. Finally, to investigate the magnetic properties of the $(Ga_{(1-x)}Fe_x)_2O_3$ alloys, a vibrating sample magnetometer (VSM) was used. Fig. 14 shows the magnetization versus magnetic field (M—H) of $(Ga_{1-x}Fe_x)_2O_3$ for the x = 0.0, 0.02 thin films having thicknesses of 106.48 nm and 131.22 nm, respectively. Diamagnetic contributions due to the sapphire substrates and sample holder rod were subtracted from the raw data. β-Ga_2O_3 demonstrates paramagnetic behavior, while for an 2% Fe content the alloy shows ferromagnetic behavior at room temperature with the observation of hysteresis. The saturation magnetization, normalized remanence (M_r/M_s), and coercivity are 4.67 emu/cm^3, 0.8769/4.67 and 56.159 (Oe) respectively. All samples with Fe concentrations below 15% also show hysteresis similar to that shown in Fig. 14. Samples with higher Fe concentration does not show hysteresis. More detailed measurements are currently being planned to understand this phenomenon. Fe doped magnetic properties of multilayer $Ga_2O_3/(Ga_{1-x}Fe_x)_2O_3$, (x 2.44%) thin films were studied by Daoyou Guo et al. [33]. They found a much larger magnetic saturation (32.8 emu/cm^3) than our experimental values (4.67 emu/cm^3). However, their alloys were formed by growing alternate layers of Fe and Ga_2O_3 which could have resulted in Fe_2O_3 in the structure. The origin of the magnetic properties is not clearly understood. Our theoretical DFT simulations have shown a magnetic moment of ~ 4.25 μ_B per Fe^{2+} atom which is comparable to the experimental value 3.22μ_B per atom, which may suggest the experimental value could be attributed to Fe in Ga_2O_3. Besides, the magnetic properties in thin films Ga_2O_3 with other elemental doping, for example Mn, Cr, have been reported elsewhere [58,72]. This study suggests $(Ga_{1-x}Fe_x)_2O_3$ as a potential candidate for future spintronic applications capable of room temperature operation.

4. Conclusions

In summary, we performed a systematic study of $(Ga_{1-x}Fe_x)_2O_3$ thin film alloys grown using PLD. An increase in the Fe content increases the lattice constant and decreases the optical bandgap as well as introduces intermediate bands. This was attributed to a change in the oxidation states of the Fe atoms based on the deposition conditions used. The trend in variation of the experimental bandgap is supported by DFT calculations. High Fe content (x = 0.4, 0.5) in the thin films also transforms the crystal structure from monoclinic to a cubic gamma phase for samples grown at 700 °C and 2.2×10^{-2} torr. Similarly, low oxygen pressure causes phase transformation from monoclinic to cubic (x = 0.15). For x = 0.4 and 0.5 the estimated refractive index at 632 nm is 2.1857 and 2.2494 respectively which are larger than the refraction index of 1.93 for β-Ga_2O_3 supporting the formation of the gamma phase for these high Fe concentrations. In addition, theoretical calculations suggest that at high Fe content, the stabilization of monoclinic phase decreases over the gamma phase. Finally, ferromagnetic properties were observed for the alloy containing Fe, representing a potential candidate for future wide bandgap dilute magnetic applications.

CRediT authorship contribution statement

Md Dalim Mia: Sample preparation, characterization, analysis and writing original manuscript draft. **Brian C Samuels:** Characterization and analysis. **Md Abdul Ahad Talukder:** Characterization and analysis. **Pablo D. Borges:** DFT calculations and analysis. **Luisa Scolfaro:**

Supervision of DFT calculations and analysis. **Wilhelmus J. Geerts:** Analysis, discussion and supervision. **Ravi Droopad:** Overall supervision, writing, reviewing and editing.

Declaration of Competing Interest

The authors declare that they have no known competing financial interests or personal relationships that could have appeared to influence the work reported in this paper.

Acknowledgement

Research was sponsored by the Army Research Office and was accomplished under Grant Number W911NF-20-1-0298.

Data availability statement

The data that supports the findings of this study are available within the article.

References

[1] M. Higashiwaki and G. H. Jessen, "Guest Editorial: The dawn of gallium oxide microelectronics," Applied Physics Letters, vol. 112, no. 6. American Institute of Physics Inc., p. 060401, Feb. 05, 2018, doi: 10.1063/1.5017845.

[2] S. Bhandari, M.E. Zvanut, J.B. Varley, Optical absorption of Fe in doped Ga_2O_3, J. Appl. Phys. 126 (16) (2019) 165703, https://doi.org/10.1063/1.5124825.

[3] A. Mauze, Y. Zhang, T. Mates, F. Wu, J.S. Speck, Investigation of unintentional Fe incorporation in (010) β-Ga_2O_3 films grown by plasma-assisted molecular beam epitaxy, Appl. Phys. Lett. 115 (5) (2019) 052102, https://doi.org/10.1063/1.5096183.

[4] B. Mallesham, S. Roy, S. Bose, A.N. Nair, S. Sreenivasan, V. Shutthanandan, C. V. Ramana, Crystal Chemistry, Band-Gap Red Shift, and Electrocatalytic Activity of Iron-Doped Gallium Oxide Ceramics, ACS Omega 5 (1) (2020) 104–112, https://doi.org/10.1021/acsomega.9b01604.

[5] I. Hany, G.e. Yang, C.E. Zhou, C. Sun, K. Gundogdu, D. Seyitliyev, E.O. Danilov, F. N. Castellano, D. Sun, E. Vetter, Low temperature cathodoluminescence study of Fe-doped β-Ga_2O_3, Mater. Lett. 257 (2019) 126744, https://doi.org/10.1016/j.matlet.2019.126744.

[6] A. D. K. Marko J. Tadjer, z John L. Lyons, Neeraj Nepal, Jaime A. Freitas Jr. and and G. M. Foster, "Review-Theory and Characterization of Doping and Defects in β-Ga 2 O 3," 2016, doi: 10.1149/2.0341907jss.

[7] S. J. Pearton et al., "A review of Ga2O3 materials, processing, and devices," Applied Physics Reviews, vol. 5, no. 1. American Institute of Physics Inc., p. 011301, Mar. 01, 2018, doi: 10.1063/1.5006941.

[8] J.B. Varley, J.R. Weber, A. Janotti, C.G. Van De Walle, Oxygen vacancies and donor impurities in β-Ga_2O_3, Appl. Phys. Lett. 97 (14) (2010) 97–100, https://doi.org/10.1063/1.3499306.

[9] S. J. Pearton, F. Ren, M. Tadjer, and J. Kim, "Perspective: Ga2O3 for ultra-high power rectifiers and MOSFETS," Journal of Applied Physics, vol. 124, no. 22. American Institute of Physics Inc., Dec. 14, 2018, doi: 10.1063/1.5062841.

[10] F. Alema, B. Hertog, O. Ledyaev, D. Volovik, G. Thoma, R. Miller, A. Osinsky, P. Mukhopadhyay, S. Bakhshi, H. Ali, W.V. Schoenfeld, Solar blind photodetector based on epitaxial zinc doped Ga_2O_3 thin film, Phys. status solidi 214 (5) (2017) 1600688, https://doi.org/10.1002/pssa.201600688.

[11] X.H. Wang, F.B. Zhang, K. Saito, T. Tanaka, M. Nishio, Q.X. Guo, Electrical properties and emission mechanisms of Zn-doped β-Ga_2O_3 films, J. Phys. Chem. Solids 75 (11) (Nov. 2014) 1201–1204, https://doi.org/10.1016/j.jpcs.2014.06.005.

[12] M. Handwerg, R. Mitdank, Z. Galazka, S.F. Fischer, Temperature-dependent thermal conductivity and diffusivity of a Mg-doped insulating β-Ga_2O_3 single crystal along [100], [010] and [001], Semicond. Sci. Technol. 31 (12) (2016) 125006, https://doi.org/10.1088/0268-1242/31/12/125006.

[13] Y.P. Qian, D.Y. Guo, X.L. Chu, H.Z. Shi, W.K. Zhu, K. Wang, X.K. Huang, H. Wang, S.L. Wang, P.G. Li, X.H. Zhang, W.H. Tang, Mg-doped p-type β-Ga_2O_3 thin film for solar-blind ultraviolet photodetector, Mater. Lett. 209 (2017) 558–561, https://doi.org/10.1016/j.matlet.2017.08.052.

[14] A.Y. Polyakov, N.B. Smirnov, I.V. Shchemerov, S.J. Pearton, F. Ren, A.V. Chernykh, A.I. Kochkova, Electrical properties of bulk semi-insulating β-Ga_2O_3 (Fe), Appl. Phys. Lett. 113 (14) (2018) 142102, https://doi.org/10.1063/1.5051986.

[15] H. He, W. Li, H. Xing, and E. Liang, "First principles study on the electronic properties of Cr, Fe, Mn and Ni doped β-Ga2O3," 2012, doi: 10.4028/www.scientific.net/AMR.535-537.36.

[16] Z. Galazka, K. Irmscher, R. Uecker, R. Bertram, M. Pietsch, A. Kwasniewski, M. Naumann, T. Schulz, R. Schewski, D. Klimm, M. Bickermann, On the bulk β-Ga_2O_3 single crystals grown by the Czochralski method, J. Cryst. Growth 404 (2014) 184–191, https://doi.org/10.1016/j.jcrysgro.2014.07.021.

[17] Y. Huang, H. Wu, Y. Zhi, Y. Huang, D. Guo, Z. Wu, P. Li, Z. Chen, W. Tang, High-insulating β-Ga_2O_3 thin films by doping with a valence controllable Fe element, Appl. Phys. A Mater. Sci. Process. 124 (9) (2018), https://doi.org/10.1007/s00339-018-2037-z.

[18] S. Mukherjee, A. Roy, S. Auluck, R. Prasad, R. Gupta, A. Garg, Room temperature nanoscale ferroelectricity in magnetoelectric $GaFeO_3$ epitaxial thin films, Phys. Rev. Lett. 111 (8) (Aug. 2013), 087601, https://doi.org/10.1103/PhysRevLett.111.087601.

[19] T. Katayama, S. Yasui, Y. Hamasaki, T. Shiraishi, A. Akama, T. Kiguchi, M. Itoh, Ferroelectric and Magnetic Properties in Room-Temperature Multiferroic $Ga_xFe_{2-x}O_3$ Epitaxial Thin Films, Adv. Funct. Mater. 28 (2) (2018) 1704789, https://doi.org/10.1002/adfm.v28.210.1002/adfm.201704789.

[20] S.H. Oh, J.H. Lee, R.H. Shin, Y. Shin, C. Meny, W. Jo, Room-temperature polarization switching and antiferromagnetic coupling in epitaxial (Ga, Fe_j2_o3/$SrRu_o3$ heterostructures, Appl. Phys. Lett. 106 (14) (2015) 142902, https://doi.org/10.1063/1.4917249.

[21] Y. Hamasaki, T. Shimizu, H. Taniguchi, T. Taniyama, S. Yasui, M. Itoh, Epitaxial growth of metastable multiferroic $AlFeO_3$ film on $SrTiO_3$ (111) substrate, Appl. Phys. Lett. 104 (8) (2014) 082906, https://doi.org/10.1063/1.4866798.

[22] M. Gich, I. Fina, A. Morelli, F. Sánchez, M. Alexe, J. Gàzquez, J. Fontcuberta, A. Roig, Multiferroic Iron Oxide Thin Films at Room Temperature, Adv. Mater. 26 (27) (2014) 4645–4652, https://doi.org/10.1002/adma.v26.2710.1002/adma.201400990.

[23] W. Kim, J. H. We, S. J. Kim, and C. S. Kim, "Effects of cation distribution for AFeO3 (A= Ga,Al)," in Journal of Applied Physics, May 2007, vol. 101, no. 9, p. 09M515, doi: 10.1063/1.2712819.

[24] M. B. Mohamed, A. Senyshyn, H. Ehrenberg, and H. Fuess, "Structural, magnetic, dielectric properties of multiferroic GaFeO3 prepared by solid state reaction and sol-gel methods," Journal of Alloys and Compounds, vol. 492, no. 1–2. pp. L20–L27, Mar. 04, 2010, doi: 10.1016/j.jallcom.2009.11.099.

[25] T. Arima et al., "Structural and magnetoelectric properties of Ga2-xFexO3 single crystals grown by a floating-zone method," Phys. Rev. B - Condens. Matter Mater. Phys., vol. 70, no. 6, p. 064426, Aug. 2004, doi: 10.1103/PhysRevB.70.064426.

[26] A. B. and V. G. S. Kavita Sharma, V Raghavendra Reddy1, Deepti Kothari, Ajay Gupta, Low temperature Raman and high field 57Fe Mossbauer study of polycrystalline $GaFeO_3$, *J. Phys.: Condens. Matter*, Mar. (2010), https://doi.org/10.1088/0953-8984.

[27] A. B. and A. M. A. Kavita Sharma, V Raghavendra Reddy, Ajay Gupta, Magnetic and 57Fe Mössbauer study of magneto-electric $GaFeO_3$ prepared by the sol–gel route, *J. Phys.: Condens. Matter*, Jan. (2013), https://doi.org/10.1088/0953-8984.

[28] Z.H. Sun, S. Dai, Y.L. Zhou, L.Z. Cao, Z.H. Chen, Elaboration and optical properties of $GaFeO_3$ thin films, Thin Solid Films 516 (21) (Sep. 2008) 7433–7436, https://doi.org/10.1016/j.tsf.2008.02.054.

[29] Z.H. Sun, Y.L. Zhou, S.Y. Dai, L.Z. Cao, Z.H. Chen, Preparation and properties of $GaFeO_3$ thin films grown at various oxygen pressures by pulsed laser deposition, Appl. Phys. A Mater. Sci. Process. 91 (1) (Apr. 2008) 97–100, https://doi.org/10.1007/s00339-007-4364-3.

[30] Morgan Trassin, Nathalie Viart, Gilles Versini, Sophie Barre, Geneviève Pourroy, Jihye Lee, William Jo, Karine Dumesnil, Catherine Dufour, Sylvie Robert, Room temperature ferrimagnetic thin films of the magnetoelectric $Ga_{2-x}Fe_xO_3$, J. Mater. Chem. 19 (46) (2009) 8876, https://doi.org/10.1039/b913359c.

[31] M. Trassin et al., "Epitaxial thin films of multiferroic GaFeO3 on conducting indium tin oxide (001) buffered yttrium-stabilized zirconia (001) by pulsed laser deposition," Appl. Phys. Lett., vol. 91, no. 20, p. 202504, Nov. 2007, doi: 10.1063/1.2813020.

[32] Darshan C. Kundaliya, S.B. Ogale, S. Dhar, K.F. McDonald, E. Knoesel, T. Osedach, S.E. Lofland, S.R. Shinde, T. Venkatesan, Large second-harmonic kerr rotation in $GaFeO_3$ thin films on YSZ buffered silicon, J. Magn. Magn. Mater. 299 (2) (2006) 307–311, https://doi.org/10.1016/j.jmmm.2005.04.017.

[33] Daoyou Guo, Yuehua An, Wei Cui, Yusong Zhi, Xiaolong Zhao, Ming Lei, Linghong Li, Peigang Li, Zhenping Wu, Weihua Tang, Epitaxial growth and magnetic properties of ultraviolet transparent $Ga_2O_3/(Ga_{1-x}Fe_x)_2O_3$ multilayer thin films, Sci. Rep. 6 (1) (2016), https://doi.org/10.1038/srep25166.

[34] K. Sharma, V. Raghavendra Reddy, A. Gupta, R. J. Choudhary, D. M. Phase, and V. Ganesan, "Study of site-disorder in epitaxial magneto-electric GaFeO3 thin films," Appl. Phys. Lett., vol. 102, no. 21, p. 212401, May 2013, doi: 10.1063/1.4807757.

[35] Yuanqi Huang, Ang Gao, Daoyou Guo, Xia Lu, Xiao Zhang, Yalei Huang, Jie Yu, Shan Li, Peigang Li, Weihua Tang, Fe doping-stabilized γ-Ga_2O_3 thin films with a high room temperature saturation magnetic moment, J. Mater. Chem. C 8 (2) (2020) 536–542, https://doi.org/10.1039/C9TC05823K.

[36] J.C.A. Huang, H.S. Hsu, Y.M. Hu, C.H. Lee, Y.H. Huang, M.Z. Lin, Origin of ferromagnetism in ZnO/CoFe multilayers: Diluted magnetic semiconductor or clustering effect? Appl. Phys. Lett. 85 (17) (Oct. 2004) 3815–3817, https://doi.org/10.1063/1.1812844.

[37] J. Chovan, E.G. Kavousanaki, I.E. Perakis, Ultrafast light-induced magnetization dynamics in ferromagnetic semiconductors, Phys. Rev. Lett. 96 (5) (2005) Aug, https://doi.org/10.1103/PhysRevLett.96.057402.

[38] Hidemi Toyosaki, Tomoteru Fukumura, Yasuhiro Yamada, Kiyomi Nakajima, Toyohiro Chikyow, Tetsuya Hasegawa, Hideomi Koinuma, Masashi Kawasaki, Anomalous Hall effect governed by electron doping in a room-temperature transparent ferromagnetic semiconductor, Nat. Mater. 3 (4) (2004) 221–224, https://doi.org/10.1038/nmat1099.

[39] S. Zhang et al., "Enhancement of longitudinal magneto-optical Kerr effect in HfO 2/Co/HfO2/Al/silicon thin films," Opt. Commun., vol. 321, pp. 226–229, Jun. 2014, doi: 10.1016/j.optcom.2014.02.010.

[40] W. Zheng, A.T. Hanbicki, B.T. Jonker, G. Lüpke, Control of magnetic contrast with nonlinear magneto-plasmonics, Sci. Rep. 4 (1) (Aug. 2014) 1–5, https://doi.org/10.1038/srep06191.

[41] P. Hohenberg, W. Kohn, Inhomogeneous electron gas, Phys. Rev. 136 (3B) (1964) B864–B871, https://doi.org/10.1103/PhysRev.136.B864.

[42] W. Kohn and L. J. Sham, "Self-consistent equations including exchange and correlation effects," Phys. Rev., vol. 140, no. 4A, p. A1133, Nov. 1965, doi: 10.1103/PhysRev.140.A1133.

[43] G. Kresse and J. Furthmüller, "Efficient iterative schemes for ab initio total-energy calculations using a plane-wave basis set," Phys. Rev. B - Condens. Matter Mater. Phys., vol. 54, no. 16, pp. 11169–11186, Oct. 1996, doi: 10.1103/PhysRevB.54.11169.

[44] J.P. Perdew, K. Burke, M. Ernzerhof, Generalized gradient approximation made simple, Phys. Rev. Lett. 77 (18) (Oct. 1996) 3865–3868, https://doi.org/10.1103/PhysRevLett.77.3865.

[45] A. Janotti, D. Segev, and C. G. Van De Walle, "Effects of cation d states on the structural and electronic properties of III-nitride and II-oxide wide-band-gap semiconductors," Phys. Rev. B - Condens. Matter Mater. Phys., vol. 74, no. 4, p. 045202, Jul. 2006, doi: 10.1103/PhysRevB.74.045202.

[46] F. Tran, P. Blaha, Accurate band gaps of semiconductors and insulators with a semilocal exchange-correlation potential, Phys. Rev. Lett. 102 (22) (Jun. 2009), 226401, https://doi.org/10.1103/PhysRevLett.102.226401.

[47] K. E. Lipinska-Kalita, P. E. Kalita, O. A. Hemmers, and T. Hartmann, "Equation of state of gallium oxide to 70 GPa: Comparison of quasihydrostatic and nonhydrostatic compression," Phys. Rev. B - Condens. Matter Mater. Phys., vol. 77, no. 9, p. 094123, Mar. 2008, doi: 10.1103/PhysRevB.77.094123.

[48] M.G. Brik, A. Suchocki, A. Kamińska, Lattice parameters and stability of the spinel compounds in relation to the ionic radii and electronegativities of constituting chemical elements, Inorg. Chem. 53 (10) (May 2014) 5088–5099, https://doi.org/10.1021/ic500200a.

[49] S. Yan, K. Liu, G. Lv, Z. Fan, Fluorine doping inducing high temperature ferromagnetism in $(In_{1-x}Fe_x)_2O_3$, J. Alloy. Compd. 551 (Feb. 2013) 40–43, https://doi.org/10.1016/j.jallcom.2012.10.024.

[50] M. Ji, X. Zhang, J. Wang, S.E. Park, Ethylbenzene dehydrogenation with CO_2 over Fe-doped $MgAl_2O_4$ spinel catalysts: Synergy effect between Fe 2+ and Fe3+, J. Mol. Catal. A: Chem. 371 (May 2013) 36–41, https://doi.org/10.1016/j.molcata.2013.01.025.

[51] T. Yamashita, P. Hayes, Analysis of XPS spectra of Fe^{2+} and Fe^{3+} ions in oxide materials, Appl. Surf. Sci. 254 (8) (Feb. 2008) 2441–2449, https://doi.org/10.1016/j.apsusc.2007.09.063.

[52] I. Uhlig, R. Szargan, H.W. Nesbitt, K. Laajalehto, Surface states and reactivity of pyrite and marcasite, Appl. Surf. Sci. 179 (1–4) (Jul. 2001) 222–229, https://doi.org/10.1016/S0169-4332(01)00283-5.

[53] Mark C. Biesinger, Brad P. Payne, Andrew P. Grosvenor, Leo W.M. Lau, Andrea R. Gerson, Roger St.C. Smart, Resolving surface chemical states in XPS analysis of first row transition metals, oxides and hydroxides: Cr, Mn, Fe, Co and Ni, Appl. Surf. Sci. 257 (7) (2011) 2717–2730, https://doi.org/10.1016/j.apsusc.2010.10.051.

[54] S.J. Roosendaal, B. Van Asselen, J.W. Elsenaar, A.M. Vredenberg, F.H.P. M. Habraken, The oxidation state of Fe(100) after initial oxidation in O_2, Surf. Sci. 442 (3) (Dec. 1999) 329–337, https://doi.org/10.1016/S0039-6028(99)01006-7.

[55] R.D. Shannon, Revised effective ionic radii and systematic studies of interatomic distances in halides and chalcogenides, Acta Crystallogr. Sect. A 32 (5) (Sep. 1976) 751–767, https://doi.org/10.1107/S0567739476001551.

[56] Zhenping Wu, Gongxun Bai, Yingyu Qu, Daoyou Guo, Linghong Li, Peigang Li, Jianhua Hao, Weihua Tang, Deep ultraviolet photoconductive and near-infrared luminescence properties of Er^{3+}-doped β -Ga_2O_3 thin films, Appl. Phys. Lett. 108 (21) (2016) 211903, https://doi.org/10.1063/1.4952618.

[57] Hiroyuki Hayashi, Rong Huang, Hidekazu Ikeno, Fumiyasu Oba, Satoru Yoshioka, Isao Tanaka, Saki Sonoda, Room temperature ferromagnetism in Mn-doped γ-Ga_2O_3 with spinel structure, Appl. Phys. Lett. 89 (18) (2006) 181903, https://doi.org/10.1063/1.2369541.

[58] Daoyou Guo, Zhenping Wu, Yuehua An, Xiaojiang Li, Xuncai Guo, Xulong Chu, Changlong Sun, Ming Lei, Linghong Li, Lixin Cao, Peigang Li, Weihua Tang, Room temperature ferromagnetism in $(Ga_{1-x}Mn_x)_2O_3$ epitaxial thin films, J. Mater. Chem. C 3 (8) (2015) 1830–1834, https://doi.org/10.1039/C4TC02833C.

[59] C. Adamo, V. Barone, Toward reliable density functional methods without adjustable parameters: The PBE0 model, J. Chem. Phys. 110 (13) (Apr. 1999) 6158–6170, https://doi.org/10.1063/1.478522.

[60] J. Furthmüller, F. Bechstedt, Quasiparticle bands and spectra of Ga_2O_3 polymorphs, Phys. Rev. B 93 (11) (Mar. 2016), 115204, https://doi.org/10.1103/PhysRevB.93.115204.

[61] H. He, W. Li, H. Xing, E. Liang, First principles study on the electronic properties of Cr, Fe, Mn and Ni doped β-Ga_2O_3, Advanced Materials Research 535–537 (Jun. 2012) 36–41, https://doi.org/10.4028/www.scientific.net/AMR.535-537.36.

[62] A. Luque, A. Martí, Increasing the Efficiency of Ideal Solar Cells by Photon Induced Transitions at Intermediate Levels, Phys. Rev. Lett. 78 (26) (Nov. 1997) 5014–5017, https://doi.org/10.1103/PhysRevLett.78.5014.

[63] C. Tablero, P. Wahnón, Analysis of metallic intermediate-band formation in photovoltaic materials, Appl. Phys. Lett. 82 (1) (Jan. 2003) 151–153, https://doi.org/10.1063/1.1535744.

[64] T. Soga, "Nanostructured Materials for Solar Energy Conversion." https://doi.org/10.1016/B978-0-444-52844-5.X5000-8.

[65] D.H. Kim, W. Lee, J.M. Myoung, Flexible multi-wavelength photodetector based on porous silicon nanowires, Nanoscale 10 (37) (Oct. 2018) 17705–17711, https://doi.org/10.1039/c8nr05096a.

[66] J. Li, S.T. Wu, Extended Cauchy equations for the refractive indices of liquid crystals, J. Appl. Phys. 95 (3) (Feb. 2004) 896–901, https://doi.org/10.1063/1.1635971.

[67] M. Rebien, W. Henrion, M. Hong, J.P. Mannaerts, M. Fleischer, Optical properties of gallium oxide thin films, Appl. Phys. Lett. 81 (2) (Jul. 2002) 250–252, https://doi.org/10.1063/1.1491613.

[68] A. E. Romanov, S. I. Stepanov, V. I. Nikolaev, and V. E. Bougrov, "Gallium Oxide: Properties and Applications a Review," 2016.

[69] S. Ghose et al., "Structural and optical properties of β-Ga2O3 thin films grown by plasma-assisted molecular beam epitaxy," J. Vac. Sci. Technol. B, Nanotechnol. Microelectron. Mater. Process. Meas. Phenom., vol. 34, no. 2, p. 02L109, Mar. 2016, doi: 10.1116/1.4942045.

[70] M. Rebien, W. Henrion, M. Hong, J. P. Mannaerts, and M. Fleischer, "Optical properties of gallium oxide thin films," 2002, doi: 10.1063/1.1491613.

[71] T. Oshima, T. Nakazono, A. Mukai, A. Ohtomo, Epitaxial growth of γ-Ga_2O 3 films by mist chemical vapor deposition, J. Cryst. Growth 359 (1) (Nov. 2012) 60–63, https://doi.org/10.1016/j.jcrysgro.2012.08.025.

[72] Daoyou Guo, Zhenping Wu, Peigang Li, Qianjing Wang, Ming Lei, Linghong Li, Weihua Tang, Magnetic anisotropy and deep ultraviolet photoresponse characteristics in Ga_2O_3: Cr vermicular nanowire thin film nanostructure, RSC Adv. 5 (17) (2015) 12894–12898, https://doi.org/10.1039/C4RA13813A.